Nanoscale

COMMUNICATION

View Article Online
View Journal

Cite this: DOI: 10.1039/c5nr06692a

Received 27th September 2015,
Accepted 14th November 2015

DOI: 10.1039/c5nr06692a

www.rsc.org/nanoscale

Recombination reduction on lead halide perovskite solar cells based on low temperature synthesized hierarchical TiO_2 nanorods†

Oscar A. Jaramillo-Quintero,[a,b] Mauricio Solís de la Fuente,[a] Rafael S. Sanchez,[a] Ileana B. Recalde,[a] Emilio J. Juarez-Perez,[a] Marina E. Rincón*[b] and Iván Mora-Seró*[a]

Intensive research on the electron transport material (ETM) has been pursued to improve the efficiency of perovskite solar cells (PSCs) and decrease their cost. More importantly, the role of the ETM layer is not yet fully understood, and research on new device architectures is still needed. Here, we report the use of three-dimensional (3D) TiO_2 with a hierarchical architecture based on rutile nanorods (NR) as photoanode material for PSCs. The proposed hierarchical nanorod (HNR) films were synthesized by a two-step low temperature (180 °C) hydrothermal method, and consist of TiO_2 nanorod trunks with optimal lengths of 540 nm and TiO_2 nanobranches with lengths of 45 nm. Different device configurations were fabricated with TiO_2 structures (compact layer, NR and HNR) and $CH_3NH_3PbI_3$, using different synthetic routes, as the active material. PSCs based on HNR-$CH_3NH_3PbI_3$ achieved the highest power conversion efficiency compared to PSCs with other TiO_2 structures. This result can be ascribed mainly to lower charge recombination as determined by impedance spectroscopy. Furthermore, we have observed that the $CH_3NH_3PbI_3$ perovskite deposited by the two-step route shows higher efficiency, surface coverage and infiltration within the structure of 3D HNR than the one-step $CH_3NH_3PbI_{3-x}Cl_x$ perovskite.

Introduction

The recent application of organic–inorganic perovskites to solar cells by Kojima *et al.*[1] has opened an attractive field for the easy preparation of solution-based processing solar cells at low temperature (<100 °C) for the development of suitable alternatives for energy conversion.[2–5] Moreover, due to the excellent optoelectronic properties and long diffusion length of electrons and holes, hybrid organic–inorganic lead halide perovskite materials have emerged as light harvesters for solar cells.[6–10] In the last few years, solution-processed hybrid perovskite solar cells (PSCs) have increased the reported efficiencies from 3.8% to a certified power conversion efficiency of 20.1%.[11]

The most commonly reported PSC structure consists of a perovskite layer deposited on a compact TiO_2 layer with an additional mesoporous layer of TiO_2. The mesoporous layer has been systematically used on dye sensitized solar cells (DSCs) and is proposed to promote a large surface area and good loading of the absorber.[12,13] However, its role in PSC is still under debate, with studies pointing to imposing some nucleation dynamics of perovskite growth,[14] helping in obtaining continuous perovskite layers, and influencing the selective properties of the electron transporting material (ETM).[15] Nevertheless, the existence of numerous boundaries among the nanoparticles of the porous layer increases the density of trapping sites and the probability for electron recombination. One-dimensional (1D) TiO_2 nanostructures (nanowires, nanotubes or nanorods) have been demonstrated to provide a lower charge recombination rate at the grain boundaries and a superior pathway along the long axis of 1D nanostructures for electron transport in DSCs.[16–19] Recently, substantial efforts were made towards the fabrication of a novel three-dimensional (3D) hierarchical architecture[20–23] with high surface area, fast electron transport and higher nucleation sites for the deposition of perovskite. 3D hierarchical assemblies have been prepared by chemical vapor deposition,[21] pulsed-laser deposition[22] and multistage electrospinning and hydrothermal methods.[23] Wang *et al.*[21] realized 3D TiO_2 nanostructures by surface-reaction-limited pulsed chemical vapor deposition (SPCVD) with superior photovoltaic performance compared to nanowires and nanoparticle systems owing to large surface area and charge transport properties. Unfortunately, this method needs a temperature of 600 °C during the entire growth process, even higher than those methods used to fabricate compact or nanostructured TiO_2 layers, where a high

[a]*Institute of Advanced Materials (INAM), Universitat Jaume I, 12006 Castelló, Spain. E-mail: sero@uji.es*
[b]*Instituto de Energías Renovables, Universidad Nacional Autónoma de México, Apartado Postal 34, Temixco, Mor., México 62580. E-mail: merg@ier.unam.mx*
†Electronic supplementary information (ESI) available. See DOI: 10.1039/c5nr06692a

sintering temperature (~500 °C) is usually required to crystallize the as-deposited amorphous films. A positive influence of the use of TiO_2 NRs on the stability of perovskite solar modules has also been reported.[24]

In this paper, we report low-temperature synthesized TiO_2 nanorods (NRs) and 3D hierarchical nanorods (HNRs) as ETM for PSCs. 3D HNRs were fabricated *via* two-step hydrothermal methods leading to PSCs with the maximum power conversion efficiency (PCE_{max}) of 10.52% under AM 1.5G illumination, which was higher than that of PSCs based on NRs and compact TiO_2 films. The good performance of 3D HNR PSCs was possibly due to the higher light harvesting of NR and HNR structures and to the reduction of recombination losses in HNR with respect to NR as detected by impedance spectroscopy. Hence, we developed a low-temperature process for ETM layers that give better performance than those using sintering steps, opening its application to PSCs.

Results

TiO_2 NR photoanodes were synthesized directly on FTO substrates without any template or compact layer (CL), *via* a hydrothermal method, as shown in Fig. 1a and b. Fig. 1 shows the top-view and cross sectional FESEM images of bare TiO_2 NRs with uniform length and width, nearly rectangular cross section and orderly distribution on the entire surface of the FTO substrate. 3D HNRs consist of a NR backbone that branches out into a network of smaller NRs (Fig. 1c and d). For its fabrication, the as prepared TiO_2 NR film was used as seed to grow branched TiO_2 NRs by a second-step hydrothermal modification method. Fig. 1c and d show that each TiO_2 NR is enclosed by TiO_2 nanobranches (diameter ~13 nm and length ~45 nm). The crystal structures of TiO_2 NR and 3D HNR were both consistent with a tetragonal rutile phase (PDF# 21-1276), similar to previous results[25,26] (Fig. S1†).

To fabricate efficient 3D HNR PSCs, preliminary studies were carried out with four different TiO_2 NR lengths (from 380 to 1100 nm, controlled by growth time) and different thicknesses of the spin-coated perovskite layer (obtained by different spin rates). It is worth remarking that all the films were synthesized using similar growth conditions: 180 °C and 51 mL of precursor solution and only the reaction time was changed (see the Experimental section in the ESI†). Fig. S2† shows FESEM images of the evolution of NR length as the growth time increases. After keeping the reaction for 110, 120, 125 and 130 min, the lengths of the TiO_2 NR were determined to be ~380, ~540, ~700 and ~1100 nm, respectively, see Fig. S2.†

Devices based on the configuration FTO/TiO_2 NR/$CH_3NH_3PbI_{3-x}Cl_x$/Spiro-OMeTAD/Au were prepared (Fig. 2a). In these devices, $CH_3NH_3PbI_{3-x}Cl_x$ was spin-coated onto the TiO_2 NR through a one-step solution deposition method at different spin rates (from 1000 to 4000 rpm) (see the Experimental section in the ESI†). Subsequently, a spin-coated Spiro-OMeTAD layer was used as a selective contact and a hole transport material (HTM). Finally, gold was evaporated onto the Spiro-OMeTAD to form an ohmic contact.

Fig. S3† shows the PCE values of NR PSCs obtained for each TiO_2 NR length with a different thickness of the perovskite

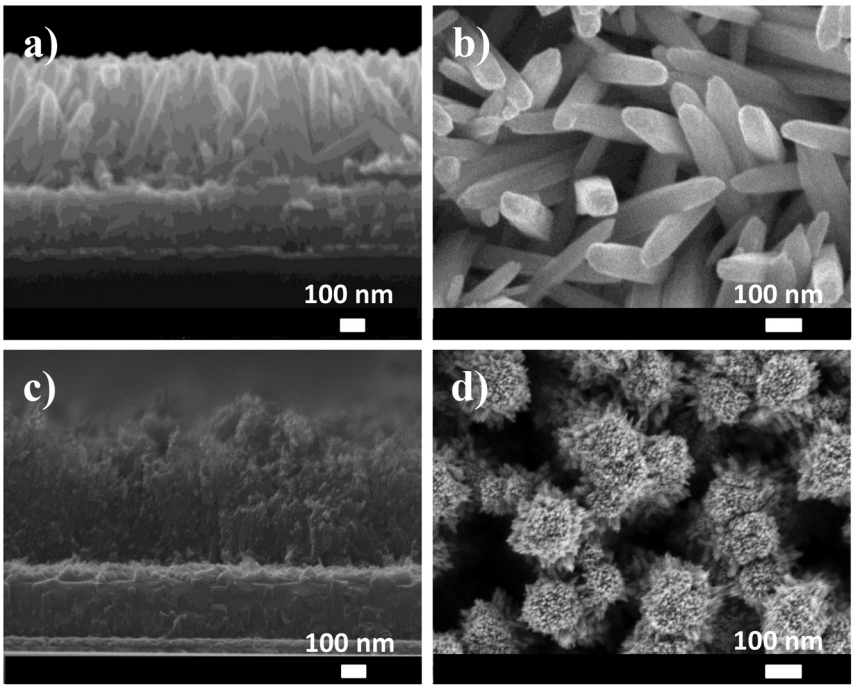

Fig. 1 (a, b) FESEM images of TiO_2 NRs and (c, d) HNRs grown by hydrothermal synthesis. (a, c) Cross-sectional view and (b, d) top-view.

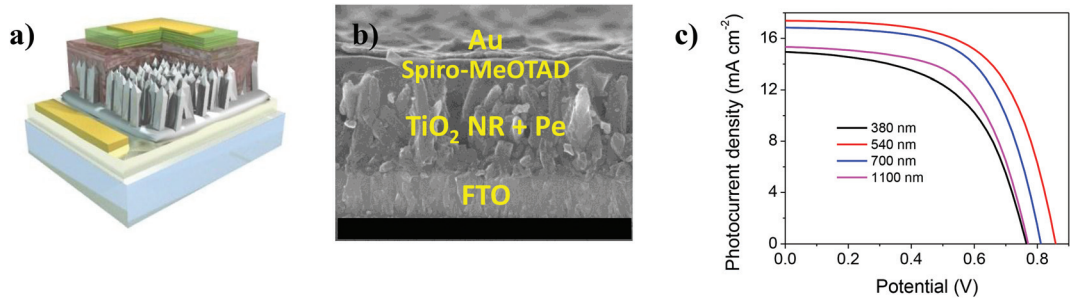

Fig. 2 (a) Device configuration showing different layers of NR PSCs. (b) Cross-sectional FESEM images corresponding to the configuration shown in (a); good penetration of perovskite into the NR structure can be appreciated. (c) *J*/*V* curves of PSCs at various nanorod lengths using a spin rate of 2000 rpm.

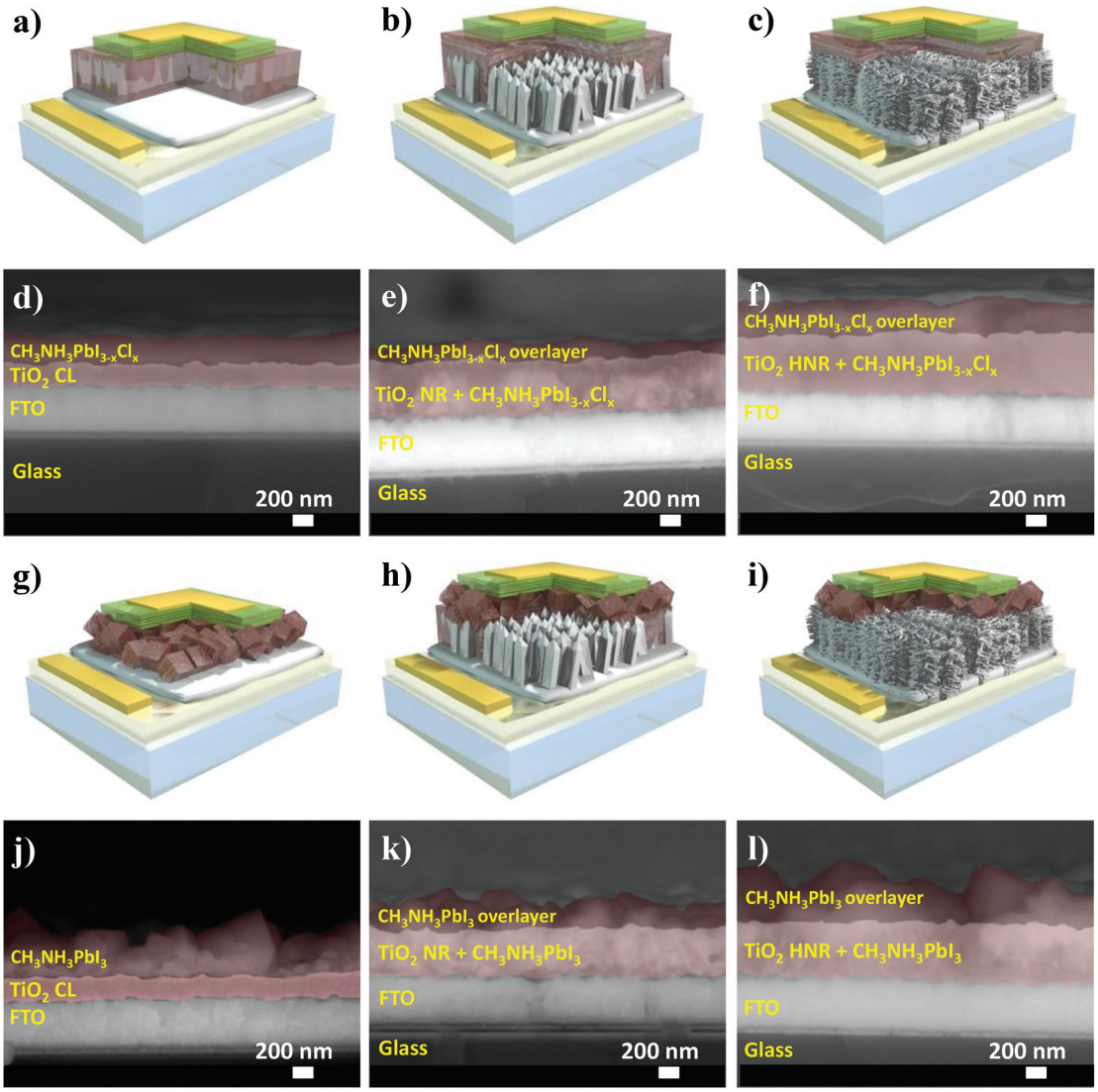

Fig. 3 Different device configurations of PSCs and cross-sectional FESEM images of TiO_2 and perovskite layers. (a, d) Flat Sing-MAICl, (b, e) NR Sing-MAICl, (c, f) HNR Sing-MAICl, (g, j) Flat Seq-MAI, (h, k) NR Seq-MAI and (i, l) HNR Seq-MAI.

layer. It can be observed that, independently of the length, all the NR showed the same optimum spin rate value for the deposition of the perovskite layer, thus obtaining the highest PCE value at 2000 rpm. A higher spin rate causes lower perovskite surface coverage and short circuit between ETM and HTM. The decrease in PCE value on increasing the spin rate is due to the lower amount of deposited perovskite and to the decrease in perovskite surface coverage, causing short circuits between ETM and HTM. The best performing current density–voltage (J/V) curves of the NR PSCs under one sun illumination are shown in Fig. 2c as a function of TiO_2 NR lengths and the related average performance parameters are listed in Table S1.† The average PCE value (PCE_{avg}) was obtained from the measurement of ten different NR PSCs. A PCE_{max} of 9.1% and a PCE_{avg} of 8.92% have been obtained for a TiO_2 NR length of 540 nm, with short circuit photocurrent density (J_{SC}) = 17.49 mA cm^{-2}, open-circuit voltage (V_{OC}) = 822.63 mV and fill factor (FF) = 0.63. Furthermore, the photovoltaic parameters were strongly dependent on the TiO_2 NR length. In general, it was found that above 600 nm NR length, the value of PCE decreases as shown in Fig. 2c and Table S1.† Previous studies using 1D TiO_2 nanostructures[25,27] suggested that this is due to charge recombination at the larger TiO_2 NR–perovskite interface.[28,29]

To demonstrate the benefits of using a 3D hierarchical architecture as a photoanode, PSCs were fabricated with a compact layer of TiO_2 (flat), bare TiO_2 NR and 3D HNR. For this study, a flat device is suited to be the control device. 3D HNR films were synthesized, as explained in the Experimental section,† using the optimum TiO_2 NRs (540 nm length) as seeds. We have also tested the influence of the perovskite growth method in the device configuration by comparing mixed-halide $CH_3NH_3PbI_{3-x}Cl_x$ perovskite (Sing-MAICl), where a single deposition step is used, and lead iodide $CH_3NH_3PbI_3$ perovskite (Seq-MAI), where two steps are utilized, see the ESI† for further experimental details. The different PSC configurations are shown in Fig. 3. Fig. 3a–c show the device configuration for Sing-MAICl PSCs, where $CH_3NH_3PbI_{3-x}Cl_x$ was deposited by a one-step technique at 2000 rpm, as described above. For Seq-MAI PSCs (Fig. 3g–i) a two-step sequential deposition method[5] was implemented. Briefly, a PbI_2 layer was spin-coated on TiO_2 photoanodes, followed by a dipping treatment in a solution of CH_3NH_3I. The same perovskite deposition procedure has been utilized for all three different

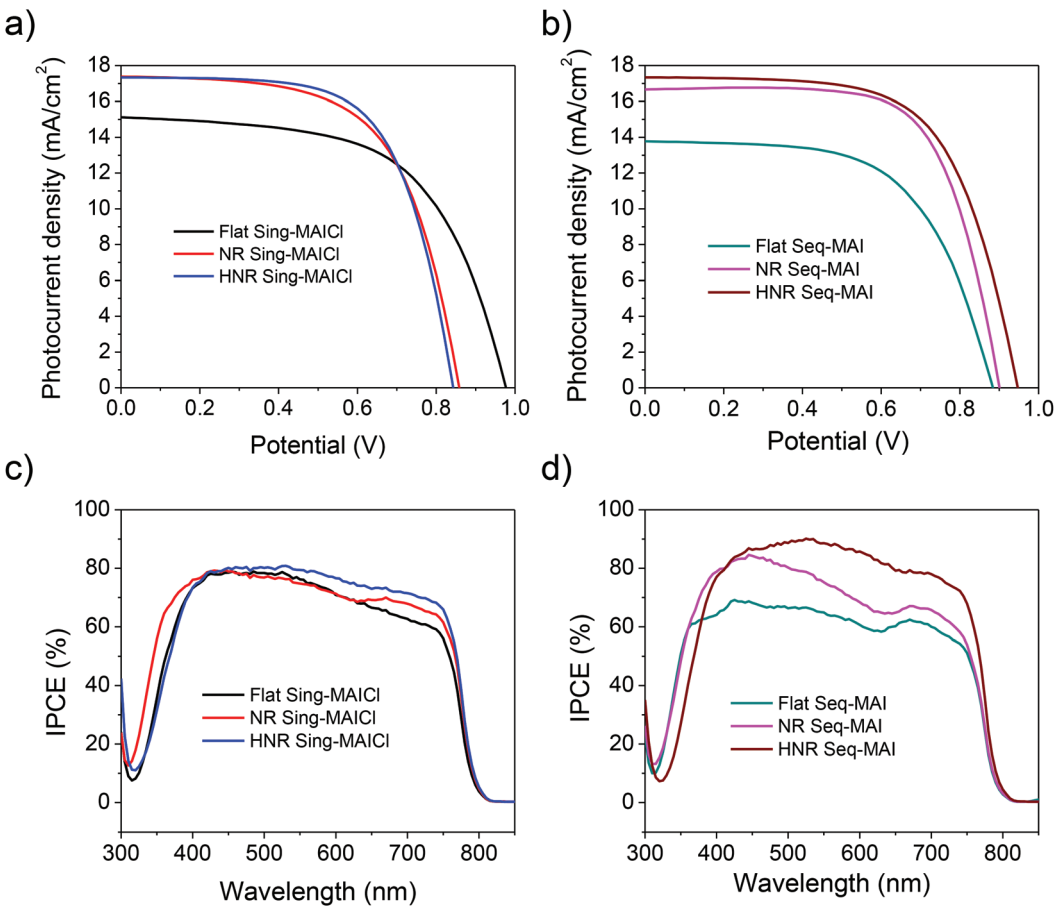

Fig. 4 J/V curves and IPCE spectra of PSCs based on different configurations. (a, c) Sing-MAICl and (b, d) Seq-MAI.

substrates, with no further optimization analysis at each particular substrate morphology.

Cross sectional FESEM images of FTO/TiO_2 NR (HNRs)/Sing-MAICl (Seq-MAI) were taken to investigate the infiltration of the perovskite within the structures of the TiO_2 NR and 3D HNR (Fig. 3e, f, k and l). We can observe the good surface coverage and infiltration of either Sing-MAICl or Seq-MAI perovskite layers within TiO_2 NR and 3D HNR photoanodes. It is important to remark that uniform coverage and adequate infiltration have been observed to be critical factors to obtain excellent photovoltaic parameters in PSCs.[30,31] Moreover, Fig. S4† shows the top-view FESEM images of the Sing-MAICl and Seq-MAI perovskite layers. The Sing-MAICl layer on Flat, NR and HNR is smooth and homogeneous and perfectly covers the TiO_2 photoanode as shown in Fig. S4a;† whereas Seq-MAI consists of cuboids (Fig. S4b†) with a grain size of ~405 nm, in agreement with the value reported for the concentration of CH_3NH_3I used.[32] In fact, sequential deposition that produces excellent results for PSCs when the TiO_2 scaffold is employed[5] does not produce good results when perovskite is deposited directly on top of the compact TiO_2 layer. Large crystals (Fig. S4b†) do not cover completely the FTO layer, producing direct contact between selective contacts (compact TiO_2 and Spiro-OMeTAD).

The effects of TiO_2 morphology on the performance of the PSCs fabricated from Flat, NR and HNR photoanodes were investigated. A summary of the photovoltaic performance and average parameters is given in Fig. 4 and Table 1. NR and HNR present higher J_{SC} than flat samples, due to a thicker perovskite layer, see Fig. 3. Except for the Sing-MAICl planar architecture, higher values are obtained for devices based on Seq-MAI, mostly because of the higher values of V_{OC}. The device with HNR Seq-MAI reached a promising maximum PCE of 10.5% resulting from J_{SC} = 17.33 mA cm^{-2}, V_{OC} = 946.96 mV and FF = 0.64. Also, HNR Sing-MAICl reports the best PCE (9.44%) among the PSCs based on the MAICl configuration, indicating that the 3D hierarchical architecture is superior to bare NR and Flat films, for the analyzed growth conditions.[21,23] Comparing the NR and HNR samples, the decrement of the incident-photon-to-current conversion efficiency (IPCE) above ~480 nm is more pronounced for PSCs based on NR (Fig. 4c and d) than those based on HNR, although the Flat device shows the highest decrement in this wavelength range. The integrated short-circuit current density $J_{SC,\ INT}$ calculated from IPCE is consistent with the J_{SC} values obtained from a solar simulator, see Table 1.

More interesting is the dependence of V_{OC} on TiO_2 morphology and perovskite type. An increase in V_{OC} with the use of 3D HNR as a photoanode instead of NR or Flat films is in accordance with previous results in the literature.[21,23] V_{OC} is strongly influenced by the recombination rate.[33] In order to study the effect of recombination on the measured devices, impedance spectroscopy under 1 Sun illumination has been carried out. Fig. 5 shows the recombination resistance, R_{rec}, obtained from impedance analysis.[34] There is a clear correlation between higher R_{rec} and higher V_{OC}. From Fig. 5a it is

Table 1 Average *J*/*V* curve parameters and standard deviation based on ten PSCs with different configurations

Device configuration	J_{SC} (mA cm^{-2})	$J_{SC,\ int}$ (mA cm^{-2})	V_{OC} (mV)	FF (%)	Efficiency (%)
Flat Sing-MAICl	14.54 ± 0.62	15.70	984.85 ± 21.11	60.24 ± 1.19	8.62 ± 0.40
NR Sing-MAICl	16.91 ± 0.65	16.38	832.77 ± 27.43	62.46 ± 1.84	8.86 ± 0.31
HNR Sing-MAICl	17.07 ± 0.83	16.82	836.42 ± 13.02	63.86 ± 0.77	9.03 ± 0.42
Flat Seq-MAI	14.56 ± 0.52	14.07	885.14 ± 13.18	54.69 ± 3.49	7.01 ± 0.44
NR Seq-MAI	16.60 ± 0.51	15.99	898.20 ± 6.58	65.10 ± 2.01	9.72 ± 0.31
HNR Seq-MAI	16.97 ± 0.23	18.11	937.99 ± 10.01	62.83 ± 1.57	10.06 ± 0.46

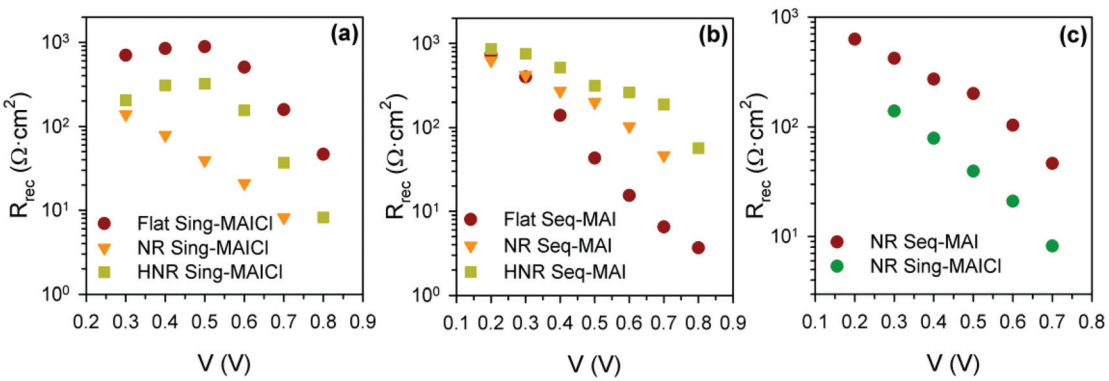

Fig. 5 Recombination resistance (R_{rec}) obtained by impedance spectroscopy for samples with (a) Sing-MAICl or (b) Seq-MAI as light harvesters. (c) Comparison of R_{rec} for NR samples using Seq-MAI and Sing-MAICl as light harvesters.

observed that for samples using Sing-MAICl, R_{rec} follows the same trend Flat > HNR > NR as V_{OC} does, see Table 1, indicating that the recombination rate increases as NR > HNR > Flat. In contrast, for Seq-MAI, see Fig. 5b, R_{rec} follows the trend HNR > NR > Flat, also in good agreement with the trend observed in the obtained V_{OC}, see Table 1. Taking into account that the recombination rate is inversely proportional to the recombination resistance,[33] the differences between Flat samples prepared by Sing-MAICl and Seq-MAI can be ascribed to the higher recombination in Flat Seq-MAI due to the incomplete covering of the compact TiO_2 surface, see Fig. S4b,† as has already been commented. Moreover, these results also point to a superior performance of HNR in comparison with NR, and also to flat samples in the case of Seq-MAI. We hypothesize that this effect could be ascribed to a lower density of surface traps in 3D HNR, which can lead to a lower net charge recombination at the TiO_2–perovskite interface, despite the larger effective surface of HNRs in comparison with NRs.

The superior performance of Seq-MAI in comparison with Sing-MAICl, except for the already analyzed case of Flat Seq-MAI, is also due to the lower recombination rate in Seq-MAI. The lower recombination observed for Seq-MAI in the case of NRs, see Fig. 5c, and in the case of HNRs, see Fig. S5,† is responsible for the higher V_{OC} observed for these samples, see Table 1. The growth method used for the synthesis of a perovskite layer also has an important effect on the device recombination and consequently on the final performance.

Conclusions

In summary, we have demonstrated an enhanced power conversion efficiency through the use of 3D hierarchical structures based on nanorods with an optimized TiO_2 NR length and Seq-MAI perovskite layers. The superior efficiency of 3D HNR as a photoanode is based, on the one hand, on the higher light harvesting properties of NR and HNR under the studied conditions, compared to flat devices. However light harvesting could be increased for flat samples with other growth conditions, but we have preferred to prepare all the samples with the same deposition procedure independently of the substrate in order to avoid introducing additional growth considerations. On the other hand the superior performance of HNR is based on the lower recombination rate obtained from HNR, especially for HNR Seq-MAI, where the recombination rate is lower than in NR samples prepared with both depositions and is even lower than in flat samples prepared with a sequential method. A lower recombination rate causes a significant increase of V_{OC} compared to the other TiO_2 structures. Further research is necessary to identify the exact recombination pathway in each configuration and the way in which HNR hinders it, despite the higher surface area. The low temperature hydrothermal routes have the additional advantage of low cost and the versatility to be implemented in other substrates, including flexible ones. More work is still needed to optimize the use of these low-cost ETMs for the preparation of PSCs with record values like those reported in the literature. Nevertheless, the results herein reported highlight the importance of the charge selective contacts for the ultimate performance of PSCs and the relationship with the recombination processes. Results also show that not only material but also the structure plays an important role in the selective contacts of PSCs. Finally, they show that advanced selective contacts with reduced recombination grown at low temperature are possible, thus paving the way for future flexible opto-electronic applications.

Acknowledgements

This work was supported by the Universitat Jaume I (project 12I361.01/1), the Spanish MINECO (project MAT2013-47192-C3-1-R), CONACYT-México (project CB-2010/153270) and UNAM (PAPIIT-IN103015). M. S. F. would like to thank CONACYT México for his postdoctoral grant. O. A. J.-Q. would like to thank CONACYT México for his Ph.D. fellowship.

References

1 A. Kojima, K. Teshima, Y. Shirai and T. Miyasaka, *J. Am. Chem. Soc.*, 2009, **131**, 6050–6051.
2 N. J. Jeon, J. H. Noh, W. S. Yang, Y. C. Kim, S. Ryu, J. Seo and S. I. Seok, *Nature*, 2015, **517**, 476–480.
3 H.-S. Kim, I. Mora-Seró, V. González-Pedro, F. Fabregat-Santiago, E. J. Juarez-Perez, N.-G. Park and J. Bisquert, *Nat. Commun.*, 2013, **4**, 2242.
4 M. M. Lee, J. Teuscher, T. Miyasaka, T. N. Murakami and H. J. Snaith, *Science*, 2012, **338**, 643–647.
5 J. Burschka, N. Pellet, S.-J. Moon, R. Humphry-Baker, P. Gao, M. K. Nazeeruddin and M. Graetzel, *Nature*, 2013, **499**, 316–319.
6 J. H. Noh, S. H. Im, J. H. Heo, T. N. Mandal and S. I. Seok, *Nano Lett.*, 2013, **13**, 1764–1769.
7 L. Bertoluzzi, R. S. Sánchez, L. Liu, J.-W. Lee, E. Mas-Marzá, H. Han, N.-G. Park, I. Mora-Seró and J. Bisquert, *Energy Environ. Sci.*, 2015, **8**, 910–915.
8 S. D. Stranks, G. E. Eperon, G. Grancini, C. Menelaou, M. J. P. Alcocer, T. Leijtens, L. M. Herz, A. Petrozza and H. J. Snaith, *Science*, 2013, **342**, 341–344.
9 K. G. Stamplecoskie, J. S. Manser and P. V. Kamat, *Energy Environ. Sci.*, 2015, **8**, 208–215.
10 Q. Lin, A. Armin, R. C. R. Nagiri, P. L. Burn and P. Meredith, *Nat. Photonics*, 2015, **9**, 106–112.
11 W. S. Yang, J. H. Noh, N. J. Jeon, Y. C. Kim, S. Ryu, J. Seo and S. I. Seok, *Science*, 2015, **348**, 1234–1237.
12 M. K. Nazeeruddin, A. Kay, I. Rodicio, R. Humphrybaker, E. Muller, P. Liska, N. Vlachopoulos and M. Grätzel, *J. Am. Chem. Soc.*, 1993, **115**, 6382–6390.
13 G. J. Meyer, *ACS Nano*, 2010, **4**, 4337–4343.

14 S. T. Williams, C.-C. Chueh and A. K.-Y. Jen, *Small*, 2015, **11**, 1–9.
15 A. Listorti, E. J. Juarez-Perez, C. Frontera, V. Roiati, L. Garcia-Andrade, S. Colella, A. Rizzo, P. Ortiz and I. Mora-Sero, *J. Phys. Chem. Lett.*, 2015, **6**, 1628–1637.
16 Y. Bai, I. Mora-Seró, F. De Angelis, J. Bisquert and P. Wang, *Chem. Rev.*, 2014, **114**, 10095–10130.
17 J. Tian, Z. Zhao, A. Kumar, R. I. Boughton and H. Liu, *Chem. Soc. Rev.*, 2014, **43**, 6920–6937.
18 X. Wang, Z. Li, J. Shi and Y. Yu, *Chem. Rev.*, 2014, **114**, 9346–9384.
19 M. C. Beard, J. M. Luther and A. J. Nozik, *Nat. Nanotechnol.*, 2014, **9**, 951–954.
20 X. Tan, P. Qiang, D. Zhang, X. Cai, S. Tan, P. Liu and W. Mai, *CrystEngComm*, 2014, **16**, 1020–1025.
21 Y. Yu, J. Li, D. Geng, J. Wang, L. Zhang, T. L. Andrew, M. S. Arnold and X. Wang, *ACS Nano*, 2015, **9**, 564–572.
22 F. Sauvage, F. Di Fonzo, A. Li Bassi, C. S. Casari, V. Russo, G. Divitini, C. Ducati, C. E. Bottani, P. Comte and M. Graetzel, *Nano Lett.*, 2010, **10**, 2562–2567.
23 K. Mahmood, B. S. Swain and A. Amassian, *Adv. Mater.*, 2015, **27**, 2859–2865.
24 A. Fakharuddin, F. Di Giacomo, A. L. Palma, F. Matteocci, I. Ahmed, S. Razza, A. D'Epifanio, S. Licoccia, J. Ismail, A. Di Carlo, T. M. Brown and R. Jose, *ACS Nano*, 2015, **9**, 8420–8429.
25 H. S. Kim, J. W. Lee, N. Yantara, P. P. Boix, S. A. Kulkarni, S. Mhaisalkar, M. Grätzel and N.-G. Park, *Nano Lett.*, 2013, **13**, 2412–2417.
26 J. Qiu, Y. Qiu, K. Yan, M. Zhong, C. Mu, He Yan and S. Yang, *Nanoscale*, 2013, **5**, 3245–3248.
27 R. Salazar, M. Altomare, K. Lee, J. Tripathy, R. Kirchgeorg, N. T. Nguyen, M. Mokhtar, A. Alshehri, S. A. Al-Thabaiti and P. Schmuki, *ChemElectroChem*, 2015, **2**, 824–828.
28 F. J. Ramos, M. Oliva-Ramirez, M. K. Nazeeruddin, M. Graetzel, A. R. González-Elipe and S. Ahmad, *J. Mater. Chem. A*, 2015, **3**, 13291–13298.
29 S. Dharani, H. K. Mulmudi, N. Yantara, P. T. Thu Trang, N.-G. Park, M. Graetzel, S. Mhaisalkar, N. Mathews and P. P. Boix, *Nanoscale*, 2014, **6**, 1675–1679.
30 J. H. Heo, S. H. Im, J. H. Noh, T. N. Mandal, C.-S. Lim, J. A. Chang, Y. H. Lee, H.-J. Kim, A. Sarkar, Md. K. Nazeeruddin, M. Graetzel and S. I. Seok, *Nat. Photonics*, 2013, **7**, 486–491.
31 T. Leijtens, B. Lauber, G. E. Eperon, S. D. Stranks and H. J. Snaith, *J. Phys. Chem. Lett.*, 2014, **5**, 1096–1102.
32 H. S. Kim and N.-G. Park, *J. Phys. Chem. Lett.*, 2014, **5**, 2927–2934.
33 F. Fabregat-Santiago, G. Garcia-Belmonte, I. Mora-Sero and J. Bisquert, *Phys. Chem. Chem. Phys.*, 2011, **13**, 9083–9118.
34 E. J. Juarez-Perez, M. Wuβler, F. Fabregat-Santiago, K. Lakus-Wollny, E. Mankel, T. Mayer, W. Jaegermann and I. Mora-Sero, *J. Phys. Chem. Lett.*, 2014, 680–685.